Quantifying Interseismic Volume Strain from Chemical Mass-Balance Analysis in Tectonic Mélanges

T. -W. Chen, A. Smye, D. Fisher, Y. Hashimoto, Hugues Raimbourg, V. Famin

Geochemistry, Geophysics, Geosystems®

RESEARCH ARTICLE
10.1029/2023GC011241

Quantifying Interseismic Volume Strain from Chemical Mass-Balance Analysis in Tectonic Mélanges

T.-W. Chen[1,2], A. Smye[1], D. Fisher[1], Y. Hashimoto[3], H. Raimbourg[4], and V. Famin[5,6]

[1]Department of Geosciences, Pennsylvania State University, University Park, University Park, PA, USA, [2]Department of Earth and Space Sciences, University of Washington, Seattle, WA, USA, [3]Department of Applied Science, Faculty of Science, Kochi University, Kochi, Japan, [4]Institut des Sciences de la Terre D'Orléans, 1A Rue de la Ferollerie Campus Géosciences, Orléans, France, [5]Université Paris Cité, Institut de Physique du Globe de Paris, Paris, France, [6]Laboratoire Géosciences Réunion, Université de La Réunion, Saint-Denis, France

Abstract Estimating interseismic deformation in subduction fault zones can offer insights into the frequency and magnitude of megathrust earthquakes. Diffusive mass transfer is a significant mechanism of strain during interseismic periods along the plate interface, observed through the pervasive scaly fabrics and mineral veins in tectonic mélanges of ancient accretionary prisms. The dissolution of fluid-mobile elements (e.g., Si and Large-Ion Lithophile Elements) along scaly folia and subsequent reprecipitation as veins lead to the enrichment of fluid-immobile elements (e.g., Ti and High Field Strength Elements) in scaly fabrics. The kinetics of dissolution-precipitation is temperature-dependent, suggesting depth-dependent mass transfer along subduction interfaces. Here, we evaluate the magnitudes of volume strain in a suite of mélange samples that span peak metamorphic temperatures of 130–340°C. Micro-chemical analysis shows that the depletion of fluid-mobile elements and enrichment of fluid-immobile elements in scaly fabrics increases with temperature. Assuming the conservation of Ti, we apply mass balance constraints to calculate the volumetric strain in scaly fabrics. Results indicate average volumetric strain of 28% and 95% in the individual scaly fabrics of the Lower Mugi and Makimine mélanges in Japan, which record temperatures near the updip and downdip isotherms bounding the seismogenic zone, respectively. To determine the total volume strain within an area of interest, we integrate the amount of volume loss along individual microstructures across the network using image analyses, which ranges from 3% to 14% for the mélanges. Our approach demonstrates the potential to fully describe the deformation related to mass transfer by connecting characterization in different scales with geochemical analyses.

Plain Language Summary Estimating how subduction fault zones deform between major earthquakes provides information about the frequency and magnitude of those earthquakes. One significant way in which deformation occurs is through the movement of substances within fault zones. We observe the evidence in rocks from ancient subduction fault zones, where substances in specific rock fabrics dissolve in fluids and reprecipitate in mineral-filled cracks. The process by which material redistributes at depth within subduction fault zones is dependent on temperature; therefore, we analyze a collection of rock samples that experienced varying temperatures. Through the examination of rock chemistry, we discover that elements carried by fluid are depleted in specific rock fabrics, while other immobile elements become enriched depending on temperature. We combine the chemistry with mathematical calculations to estimate the amount of deformation in terms of changes in rock volume. Our results reveal variations in volume loss in fabrics of rocks that experienced the lowest and highest temperatures among our samples. To obtain a comprehensive understanding of the deformation in our area of interest, we integrate the results with an analysis of rock images. Our study demonstrates how we can gain insights into the deformation occurring during these periods by combining different analytical approaches.

Key Points:

- Mass-balance analysis quantifies strain in a microstructure. Coupling with image analysis integrates strain over the area of interest
- Degrees of mass transfer vary with temperature observed in tectonic mélanges
- Single scaly fabrics exhibit >60% average volume loss, while mélanges show <20% total volume strain

Supporting Information:

Supporting Information may be found in the online version of this article.

Correspondence to:

T.-W. Chen,
txc69@psu.edu

Citation:

Chen, T.-W., Smye, A., Fisher, D., Hashimoto, Y., Raimbourg, H., & Famin, V. (2024). Quantifying interseismic volume strain from chemical mass-balance analysis in tectonic mélanges. *Geochemistry, Geophysics, Geosystems*, *25*, e2023GC011241. https://doi.org/10.1029/2023GC011241

Received 14 SEP 2023
Accepted 15 JAN 2024

Author Contributions:

Conceptualization: T.-W. Chen, A. Smye, D. Fisher
Data curation: T.-W. Chen
Formal analysis: T.-W. Chen
Funding acquisition: A. Smye, D. Fisher
Investigation: T.-W. Chen
Methodology: T.-W. Chen, A. Smye
Project administration: D. Fisher
Resources: T.-W. Chen, A. Smye, D. Fisher, Y. Hashimoto, H. Raimbourg, V. Famin
Software: T.-W. Chen, A. Smye
Supervision: A. Smye, D. Fisher

1. Introduction

Studying interseismic deformation along the plate interface is crucial for determining the recurrence intervals and energy release of megathrust earthquakes. Tectonic mélanges in exhumed accretionary prisms are considered ancient subduction fault rocks based on their lithology, stratigraphy, fabrics, and pressure-temperature (P-T) records (e.g., Kimura et al., 2012). These mélanges are interpreted as damage zones at the footwall of paleo-décollements or regional out-of-sequence thrusts (e.g., Fisher & Byrne, 1987), given the presence of cm-scale

Validation: T.-W. Chen, A. Smye, D. Fisher, H. Raimbourg, V. Famin
Visualization: T.-W. Chen
Writing – original draft: T.-W. Chen
Writing – review & editing: T.-W. Chen, A. Smye, D. Fisher, Y. Hashimoto, H. Raimbourg, V. Famin

zones of cataclastic rocks on top of them (e.g., Hashimoto et al., 2012; Ikesawa et al., 2003; Kitamura et al., 2005; Meneghini et al., 2010). During interseismic periods, plate motion is likely accommodated by diffusive mass transfer strain across 10–100-m-wide mélange zones, while coseismic slip occurs within narrow cataclasites (Fisher et al., 2021). Thus, exhumed mélange rocks provide unique materials for directly observing the interseismic deformation accumulating in subduction fault zones.

Mass transfer as a predominant style of strain has been widely observed in tectonic mélanges of the Shimanto belt in Japan (e.g., Hashimoto & Kimura, 1999; Onishi & Kimura, 1995; Ujiie, 1997) and the Kodiak accretionary complex in Alaska (e.g., Fisher & Byrne, 1987; Rowe et al., 2009; Sample & Moore, 1987). Field observations reveal a general structural pattern of anastomosing networks of scaly fabrics with polished and striated surfaces in the mudstone matrix, and mineral veins with varying occurrences in both the mudstone matrix and embedded sandstone blocks/lenses (Figure 1; e.g., Kimura & Mukai, 1991; Raimbourg et al., 2021; Ujiie, 2002). Microstructural and geochemical analyses indicate that the scaly microfaults are depleted of fluid-mobile elements (e.g., Si, Li, Al, and Large-Ion Lithophile Elements [LILEs]) and enriched in fluid-immobile elements (e.g., Ti, Rare Earth Elements and High Field Strength Elements [HFSEs]), leaving dark seams with opaque materials (Fisher & Brantley, 2014; Kawabata et al., 2007). Adjacent veins show the opposite pattern of element distribution (Ramirez et al., 2021), indicating that portions of mudstones in the mélanges have undergone metasomatic alteration and volume strain whereby mobile elements were dissolved, transported, and reprecipitated in cracks within the mélanges. Given the prevalence of scaly folia and mineral veins observed in the mélanges, it is likely that the dissolution-reprecipitation process has accommodated a significant amount of relative plate motion.

Mass transfer operating along the plate interface is a slow and continuous process in contrast to the sudden release of energy during coseismic slip. Previous models based on the kinetics of the dissolution-precipitation process have shown that the rate of crack-sealing could produce significant decreases in fracture volume during earthquake recurrence intervals (e.g., Fisher et al., 2019; Gratier et al., 2003), supporting the idea that deformation accumulates over interseismic timescales. Despite variations in assumptions and constraints across different models (see Fisher et al., 2021; Williams & Fagereng, 2022 for reviews), it is reasonable to assume that the rate of mass transfer varies with depth due to the temperature-dependence of the kinetics. The transition from seismic to aseismic behavior at the downdip end of the seismogenic zone is likely attributed to the increased amount of strain accommodated by mass transfer, which subsequently leads to a reduction in the accumulation of slip deficit. The amount of deformation observed in tectonic mélanges of ancient accretionary prisms may provide clues about the magnitude and rate of the mass transfer process. However, there is currently limited literature on directly deriving these parameters from rock records.

Quantifying deformation related to mass transfer in mélanges is challenging due to the rarity of geometric markers and the large spatially heterogeneous magnitudes of deformation. Previous attempts to estimate volumetric strain, such as Kawabata et al. (2007)'s application of the chemical isocon method, have been limited to a single tectonic mélange. Furthermore, the method requires powdering samples to obtain bulk rock compositions, which precludes the analysis of single microstructures. To address these limitations, we characterize a suite of mélange samples from the Shimanto belt and the Kodiak accretionary prism with varying paleotemperatures to compare

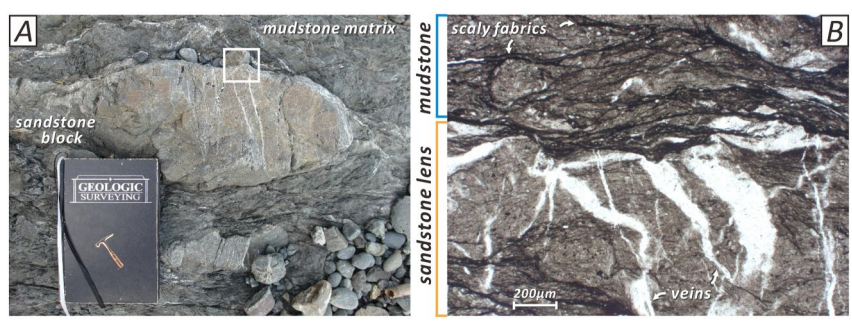

Figure 1. (a) Field photo showing the block-in-matrix texture of the Okitsu mélange in the Cretaceous Shimanto belt, Japan. (b) Photomicrograph of the Mugi mélange in the Cretaceous Shimanto belt. An intricate network of anastomosing scaly fabrics develops in the mudstone, accompanied by mineral veins that are primarily found within the embedded sandstone lens and, to a lesser extent, in the matrix.

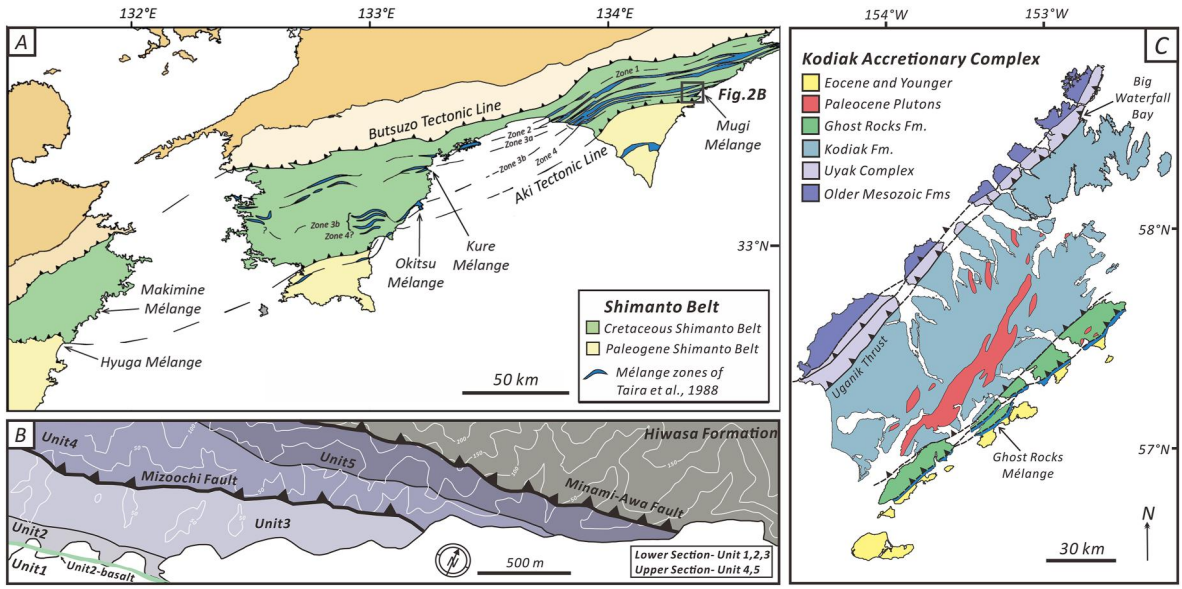

Figure 2. (a) Geological map of the Shimanto belt in Japan. The mélange units investigated in this study are located in the Cretaceous sub-belt. (b) Map of the Mugi mélange (Kitamura & Kimura, 2012), which is divided into lower and upper sections based on the paleotemperature record (Ikesawa et al., 2005). (c) Geological map of the Kodiak accretionary complex in Alaska (Fisher & Byrne, 1987).

the degrees of mass transfer under varying thermal conditions. We constructed element maps to visualize element distributions between deformed and undeformed phases and measured element concentrations in each phase to quantify volumetric strain accumulating in individual microstructures. By integrating strain over the areas of thin sections estimated from image analyses, we compare the total strain accumulated in each mélange unit and determine whether a temperature dependency exists for the mass transfer process in subduction fault zones. Our study provides a comprehensive analysis of mass transfer deformation in mélanges and sheds light on the role of temperature in the process.

2. Geological Settings

2.1. The Shimanto Belt

The Shimanto belt exposes on-land from the Kanto district in the east to the Ryukyu Islands in the west of Japan. The belt consists of a series of units that are parallel to the Nankai trench and dip in a northwestern direction with a younging trend toward the southeast. By combining biostratigraphic ages, it has been interpreted as the Cretaceous to Miocene analog of the modern Nankai accretionary prism. The Shimanto belt is further divided into two sub-belts based on differences in stratigraphic ages and timing of accretion: the Cretaceous sub-belt to the north and the Paleogene-Neogene sub-belt to the south (e.g., Taira, 1980; Figure 2a).

Each sub-belt of the Shimanto belt comprises multiple pairs of coherent overriding zones and underlying mélange zones, separated by discrete fault zones characterized by gouge and pseudotachylite (e.g., Hashimoto et al., 2012; Ikesawa et al., 2003; Kitamura et al., 2005). The coherent units are identified as trench turbidites and consist of interbedded sandstone and shale with preserved sedimentary bedding. In contrast, the mélange units exhibit disrupted fabrics with sandstone boudins embedded in a foliated mudstone matrix, along with minor lenses/blocks of basalt, tuff, and deep-sea floor sediments including radiolarian cherts and red shales. Based on the age-lithology relationships, the disrupted strata can be reconstructed to an ocean-floor stratigraphy, with the basaltic oceanic crust at the base, overlain by pelagic sediments and/or mudstones (Taira et al., 1988).

In this study, we focus on analyzing tectonic mélanges located within the Cretaceous Shimanto belt, which includes the lower and upper sections of the Mugi mélange (hereinafter referred to as Lower Mugi and Upper Mugi mélanges; Ikesawa et al., 2005; Kimura et al., 2012; Kitamura & Kimura, 2012; Kitamura et al., 2005; Matsumura et al., 2003), Kure mélange (Mukoyoshi et al., 2006), Okitsu mélange (Ikesawa et al., 2003), Hyuga mélange

(Kondo et al., 2005; Raimbourg et al., 2015, 2019), and Makimine mélange (Kitamura & Kimura, 2012; Figures 2a and 2b).

2.2. The Kodiak Accretionary Complex

The Kodiak accretionary complex, which shares similarities with the Shimanto belt, is composed of a series of accreted packages that trend northeast and dip northwest parallel to the Aleutian trench. This complex includes five accreted terranes that are separated by thrust faults, and they have been found to decrease in age seaward from the Late Cretaceous to Paleocene (Moore et al., 1983). Our study focuses on several specific mélange units within the Kodiak accretionary complex, including the Uyak complex (Byrne & Fisher, 1990; Connelly, 1978; Rowe et al., 2009), the Waterfall Bay mélange in the Kodiak Formation (Connelly, 1978; Fisher & Byrne, 1987), and the Ghost Rocks mélange in the Ghost Rocks Formation (Byrne, 1984; Fisher & Byrne, 1987). These units are located in a northwestern to southeastern sequence across the Kodiak accretionary complex.

The Uyak complex is recognized as a tectonic mélange (e.g., Connelly, 1978), whereas the Kodiak and Ghost Rocks Formations include coherently interbedded turbidites in addition to stratigraphically chaotic mélanges (e.g., Byrne, 1982, 1984; Sample & Moore, 1987). The Waterfall Bay mélange is exposed on the northwestern side of the Kodiak Formation, directly below the Uganik Thrust (Connelly, 1978; Fisher & Byrne, 1987). This fault is interpreted as a fossil out-of-sequence thrust, which brought the Uyak mélange over the Waterfall Bay mélange (Rowe et al., 2009). On the southeastern side of the Ghost Rocks Formation, the Ghost Rocks mélange occurs and is separated from the coherent unit by a paleodécollement (Byrne, 1984; Fisher & Byrne, 1987; Figure 2c).

2.3. Paleotemperature Records

The thermal evolution of the Shimanto belt and Kodiak accretionary prism have been extensively characterized using various geothermometers. The Lower Mugi mélange and Makimine mélange are widely accepted as recording the lowest and highest temperatures, respectively. Raman spectroscopy of carbonaceous material (RSCM) and vitrinite reflectance analyses of the Lower Mugi mélange indicate temperatures of 165–205°C and 130–150°C, respectively (Ikesawa et al., 2005; Raimbourg et al., 2019); fluid inclusion thermometry suggests temperatures of 125–195°C and 135–245°C, based on two generations of veins (Matsumura et al., 2003). The maximum temperatures estimated for the Makimine mélange using RSCM and vitrinite reflectance are 330–340°C and 340°C, respectively (Kiminami & Ohno, 1999; Raimbourg et al., 2021; Ujiie et al., 2018). The temperature estimates for the two mélange units correspond to the updip (100–150°C) and downdip limits (~350°C) of the seismogenic zone (Hyndman & Wang, 1993; Hyndman et al., 1997).

The Cretaceous Shimanto belt contains other mélange units with intermediate temperature records. The Upper Mugi mélange shows a thermal peak of 170–200°C based on vitrinite reflectance, leading to the interpretation that the Mizoochi Fault between the Lower and Upper Mugi mélange is a fossil out-of-sequence thrust that juxtaposes units with different thermal grades (Ikesawa et al., 2005; Figure 2b). In southwestern Shikoku, the Kure mélange records temperatures of 220–240°C according to vitrinite reflectance (Mukoyoshi et al., 2006). Further south, the Okitsu mélange experienced slightly higher maximum temperatures of 215–250°C and 265°C based on RSCM and vitrinite reflectance analyses, respectively (Raimbourg et al., 2019; Sakaguchi, 1996). Fluid inclusions in quartz and calcite veins of the mélange reveal an average temperature of 210°C (Sakaguchi, 1996). In eastern Kyushu, the Hyuga mélange recorded thermal conditions of 205–265°C, 250–270°C, and 250–300°C based on RSCM, vitrinite reflectance, and illite crystallinity, respectively (Hara & Kimura, 2008; Kondo et al., 2005; Mukoyoshi et al., 2009; Raimbourg et al., 2017, 2021). Fluid inclusion studies focusing on veins with three different occurrences indicate temperature estimates of 175–305°C (Kondo et al., 2005; Raimbourg et al., 2015, 2019).

The tectonic mélanges in the Kodiak accretionary prism also preserve a record of paleotemperatures that fall within the range expected for the seismogenic zone. The Kodiak Formation recorded a maximum burial temperature of 225°C according to vitrinite reflectance measurements (Sample & Moore, 1987), while RSCM data suggest a broad temperature range, spanning from 250 to 350°C (Raimbourg et al., 2021; Rajič et al., 2023). Fluid inclusion studies suggest a temperature range of 205–255°C based on measurements from two generations of veins (Myers & Vrolijk, 1986; Vrolijk et al., 1988). Similarly, the Ghost Rocks Formation exhibits a thermal peak of 225–250°C based on vitrinite reflectance data (Moore et al., 1983), with slightly higher values of 240–260°C

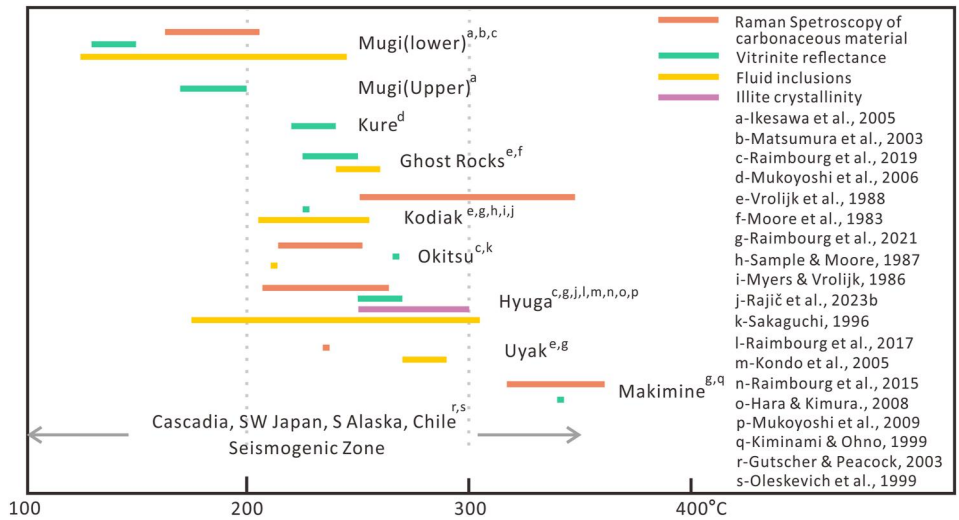

Figure 3. Plot summarizing paleotemperature records of mélange units in both the Cretaceous Shimanto belt and the Kodiak accretionary complex determined by multiple geothermometers. The range agrees with the temperatures inferred for the seismogenic zone of active convergent margins.

estimated from fluid inclusion measurements (Vrolijk et al., 1988). In the Uyak mélange, fluid inclusion studies suggest higher temperatures of 270–290°C (Vrolijk et al., 1988) compared to the RSCM estimate of 235°C (Raimbourg et al., 2021). While additional analysis is necessary to reconcile the temperature readings acquired from different geothermometers for each mélange, the compilation of reported temperature estimates shows that these mélange units collectively preserve a record of peak temperatures that span the range relevant to the seismogenic zone of modern subduction interfaces (e.g., Gutscher & Peacock, 2003; Oleskevich et al., 1999; Figure 3).

3. Petrography and Microstructures

The mélange units analyzed in this study exhibit the evidence of multiple stages of deformation, which are linked to the gradual consolidation and layer-parallel shearing occurring during subduction. The most notable feature of these units is the block-in-matrix texture, where the phyllosilicate matrix aligns with the long axes of the embedded sandstone boudins (Figures 1a and 4a). The fabric is influenced by a later stage of Y-P-R shear surfaces, where the phyllosilicates reoriented parallel to the P surfaces, exhibiting low angles to the Y surfaces. Moreover, the R planes crosscut or terminate at the margins of sandstones (Figure 4a; e.g., Fisher & Byrne, 1987; Kitamura & Kimura, 2012; Kimura et al., 2012; Kondo et al., 2005).

Shearing localizes along microfaults in the clay-rich matrix as the subduction sediments become more cohesive. Pressure solution occurs accompanying cataclasis in the microfaults, resulting in scaly fabrics characterized by seams of dark residuals with widths of a few to 10s of microns (Figures 1b and 4; e.g., Fisher & Byrne, 1987). The materials that dissolve along scaly fabrics are likely to diffuse into cracks, and precipitate as crack-sealing veins (Fisher et al., 2019; Ramirez et al., 2021). The most distinct occurrence of veins is associated with tensile cracks forming at the margins of sandstone blocks/lenses (e.g., Hashimoto et al., 2003; Matsumura et al., 2003). There is another set of veins sharing a similar orientation but crosscutting into the matrix. They are considered to have formed during the duplex underplating of mélanges that occurred after the deformation during underthrusting (e.g., Hashimoto et al., 2002). Other types of veins can also be observed parallel to the foliation or along shear surfaces (Figures 4b and 4c). The majority of veins are composed of quartz where evidence of crack-seal process is preserved including arrays of fluid inclusion bands or solid inclusion bands composed of wall rock materials (Figure 5a). Some veins consist of both quartz and calcite, with calcite grains preserved in the middle and quartz grains grown on both sides of the veins (Figure 5b). Albite and chlorite are also found in veins of several mélange units (e.g., Fisher et al., 2021; Ramirez et al., 2021).

10.1029/2023GC011241

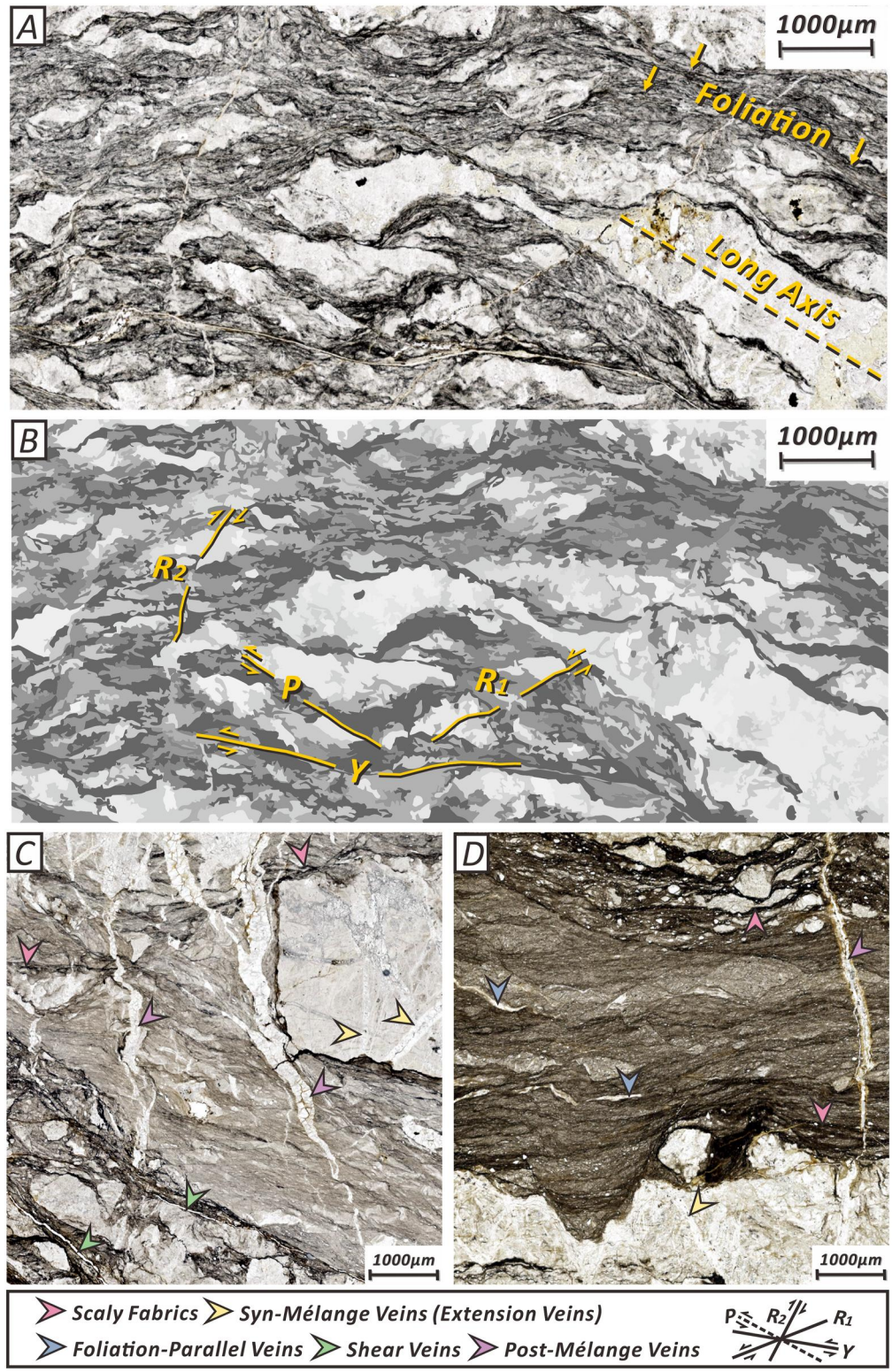

Figure 4. Photomicrographs of samples collected from (a) the Waterfall Bay mélange, (c) Hyuga mélange, and (d) Kure mélange under plane-polarized light. (a) The foliation of the mudstone matrix is marked by yellow arrows. It is parallel to the long axes of sandstones (dashed yellow line). (b) Line drawing of the photomicrograph (a), where the Y-P-R surfaces along with the shear sense are annotated. (c, d) Pink arrows indicate the scaly fabrics characterized by dark seams due to pressure solution. Yellow, blue, green, and purple arrows mark the extension veins, foliation-parallel veins, shear veins, and the post-mélange veins, respectively.

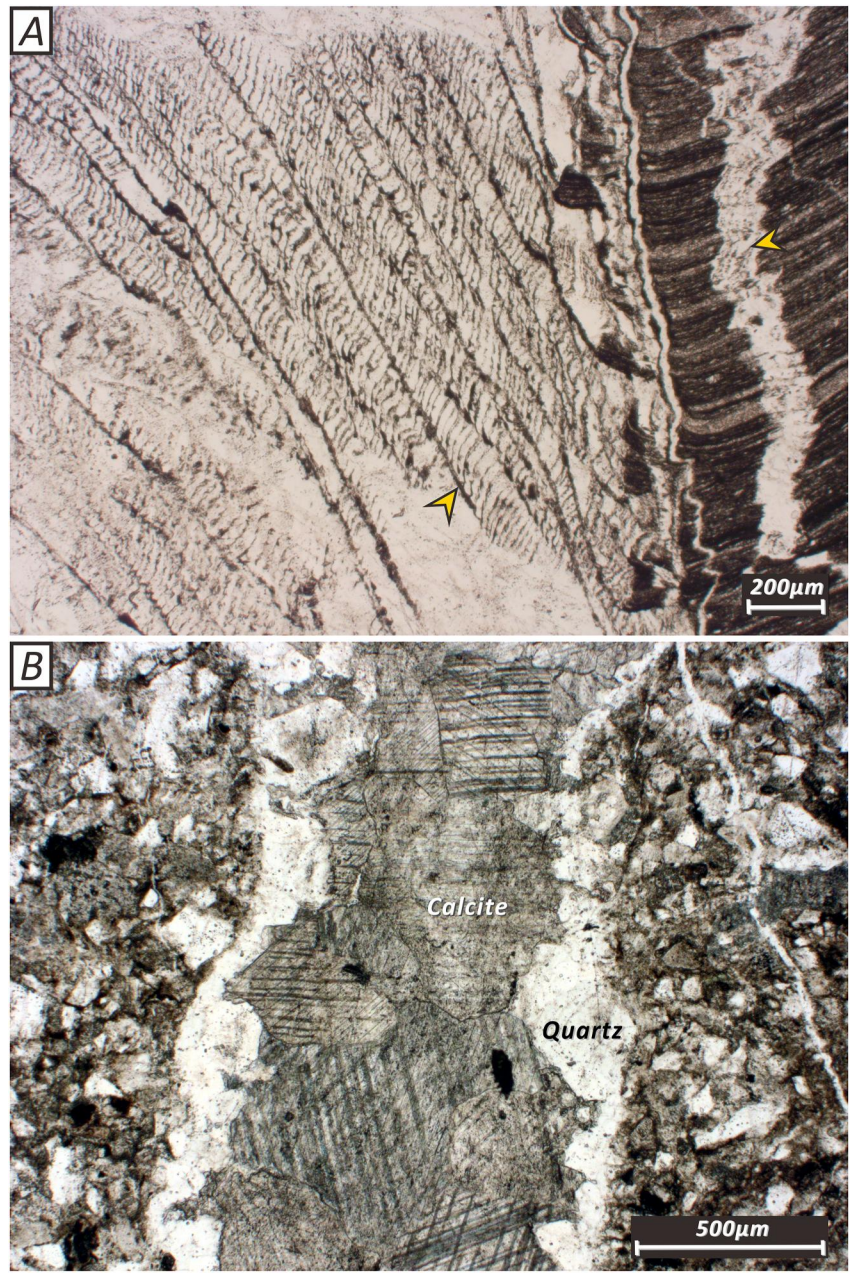

Figure 5. Photomicrographs of samples collected from (a) the Waterfall Bay mélange and (b) the Upper Mugi mélange under plane-polarized light. (a) Yellow arrows indicate inclusions of wall rocks, reflecting repeated crack-seal events along vein boundaries. (b) A vein with calcite growing in the center and quartz on the sides.

4. Analytical Methods

4.1. Electron Probe Micro Analyzer (EPMA)

A representative sample was selected from each of the six mélange units within the Cretaceous Shimanto belt as well as from the three mélange units of the Kodiak accretionary complex (Table S1). These selected samples were then prepared as standard polished thin sections. Areas with scaly fabrics and undeformed mudstone phacoids were chosen for analyses under a petrographic microscope. Major and minor element maps including Na, Mg, Al, Si, K, Ti, and Fe were produced for the areas of interest using the Cameca SX-5 Electron Probe Micro Analyzer (EPMA) at the Materials Characterization Lab at Pennsylvania State University (PSU). The EPMA was operated at 15 keV accelerating voltage and 30 nA beam current, using a stage-scanned grid of 512 × 512 pixels with a step

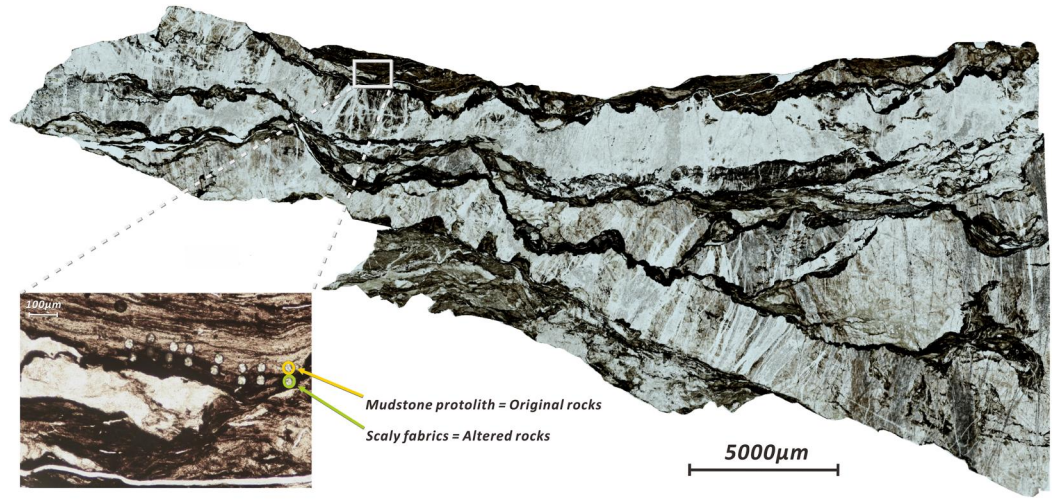

Figure 6. The scanned image of the Uyak mélange sample. Areas covering scaly fabrics and mudstone protoliths were selected for analyses. The zoomed-in image on the bottom left shows the arrays of ablation spots in the two phases respectively. Element concentrations measured at each pair of adjacent points are used to determine the local volume strain related to the alteration of mudstone protolith into scaly fabrics.

size of 5 pixels and a dwell time of 10 ms per pixel. Calibration standards including sphene for Ti, pyrope or enstatite for Mg, plagioclase for Na, orthoclase for K, olivine for Fe, and spinel for Al were used. Quantitative measurements of the same elements were conducted on several spots in the two phases of each thin section using a defocused beam size of 20 μm.

4.2. Laser Ablation Inductively Coupled Plasma Mass Spectrometry (LA-ICPMS)

A series of spots along scaly fabrics, mudstone protoliths, and veins were selected in each thin section of the nine mélange units (Figure 6). Major, minor, and trace elements were measured in situ using a Thermo Scientific iCAP-RQ ICP-MS coupled with a Teledyne/Photon Machines Analyte G2 Excimer Laser Ablation System at the *LionChron* facility in the Department of Geosciences at PSU. The laser ablation experiment was conducted with a spot size of 35 μm, fluence of 4.05 J/cm^2, 10 Hz repetition rate, and 20 s continuous ablation. Prior to analysis, the laser was first fired thrice to remove any surface contamination, and this material was allowed to wash out for ∼15 s. Basalt glass KL2G (Jochum et al., 2000) served as a primary standard; tonalite glass T1-G, rhyolite glass ATHO-G, and synthetic NIST SRM 612 glasses were used as secondary standards to evaluate the precision of the measurements. The Iolite software (Paton et al., 2011) was used to reduce the raw mass spectrometric data, including baseline correction, time-dependent laser-induced interelement fractionation, plasma-induced fractionation, and instrumental drift. To determine the concentration of each element, the abundance of Si in each textural setting measured using the EPMA was used as the internal standard. Using the same methods as applied to unknowns, and treating all whole-rock glasses besides KL2G as secondary reference materials, this routine yielded values accurate to ∼10%–15% for all elements.

4.3. Image Analysis

We utilized image analysis techniques to determine the proportions of scaly fabrics and veins in each thin section. Thin section images were acquired using a high-performance slide scanner, ZEISS Axioscan (Figures 6 and 7a), and analyzed using the scientific image-analysis program ImageJ (Abràmoff et al., 2004). The processing steps involved (a) converting the images into 8-bit grayscale, (b) applying the thresholding function to differentiate the scaly fabrics (represented as black color) from the surrounding rocks, and (c) automatically computing the percentages of scaly fabrics based on the colors (Figure 7b). The same image analysis procedure was applied to determine the percentage of mineral veins in each thin section, with the white color of the veins facilitating their differentiation from the surrounding rocks (Figure 7c).

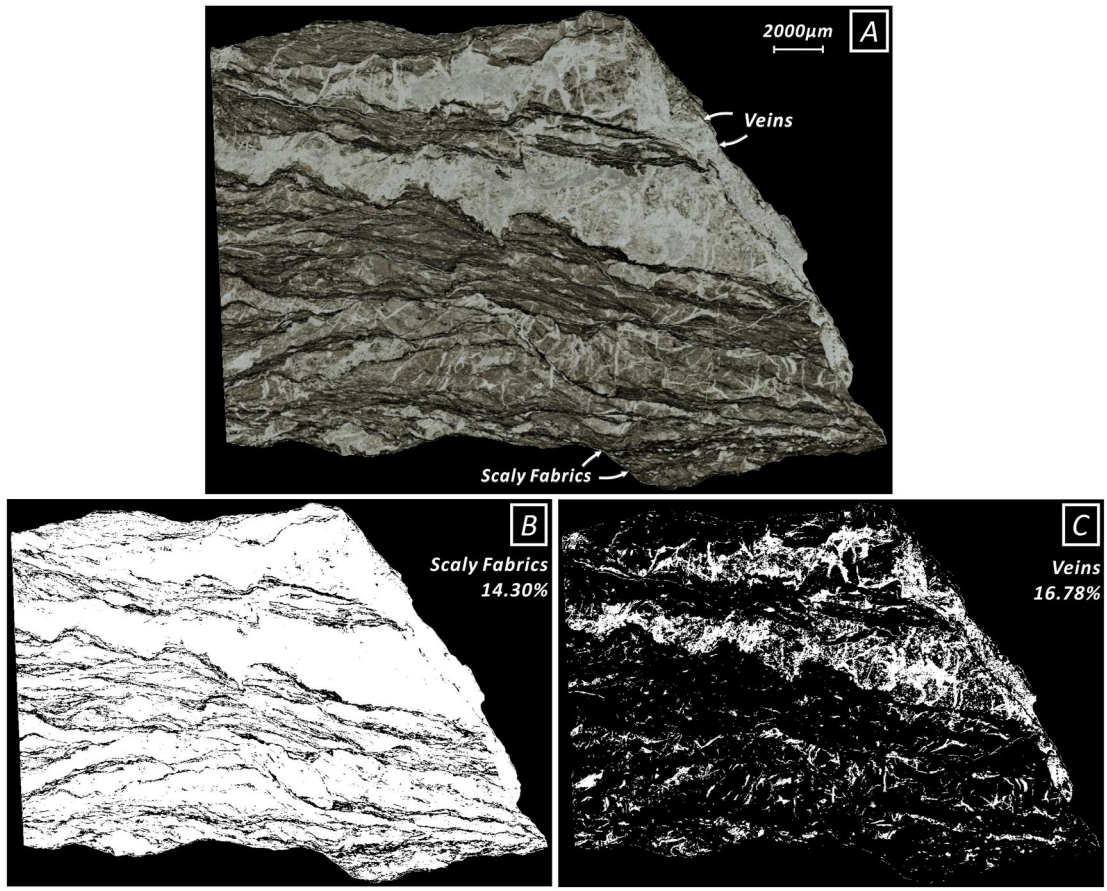

Figure 7. An example of image analysis conducted on (a) the scanned image of the Upper Mugi mélange sample. The application of the thresholding method enables the differentiation of the proportion of (b) scaly fabrics (shown as black lines) and (c) veins (shown as white lines) based on the color variance.

5. Results

5.1. EPMA Analysis

We have created a set of element maps for selected areas within six mélanges from the Cretaceous Shimanto belt and three mélanges from the Kodiak accretionary complex. These maps show the relative distribution of various elements, including Si, Ti, Al, K, Na, Fe, and Mg. Notably, the Si maps demonstrate a depletion of Si along scaly fabrics, which is apparent as blue seams compared to adjacent undeformed mudstones, manifested as green areas (Figures 8 and 9a). This depletion is more pronounced in mélange samples that have been subjected to higher temperatures, such as the Kodiak, Okitsu, Hyuga, and Uyak mélanges, as indicated by the increased blue areas (Figure 9a). In the Makimine mélange sample, while the scaly fabrics are not as extensive, the Si content is significantly reduced, as evidenced by the dark blue color along the scaly folia (Figures 8c and 9a).

Conversely, the distribution of Ti is anticorrelated with Si and is enriched along the scaly fabrics. The temperature-dependence of Ti enrichment is demonstrated by the presence of crystallized titanium oxides (colorful spots) along scaly fabrics in mélanges with higher temperature records (Figure 9b). This negative correlation between Ti and Si is in agreement with previous observations (Kawabata et al., 2007; Ramirez et al., 2021) and supports the use of Ti as a conservative reference element for mass balance calculations.

Like Si, Al is a major component of the mudstone matrix, shown as red areas on the Al maps. Its relative depletion along scaly fabrics appears as blue lines on the maps, suggesting its mobility (Figure 8 and Figure S1 in Supporting Information S1). K exhibits a similar pattern (Figure 8 and Figure S2 in Supporting Information S1). It is noteworthy that the high Si, Al, and K contents in the undeformed mudstones of the Makimine mélange sample indicate the formation of muscovite due to a slightly higher grade of metamorphism than other mélange units

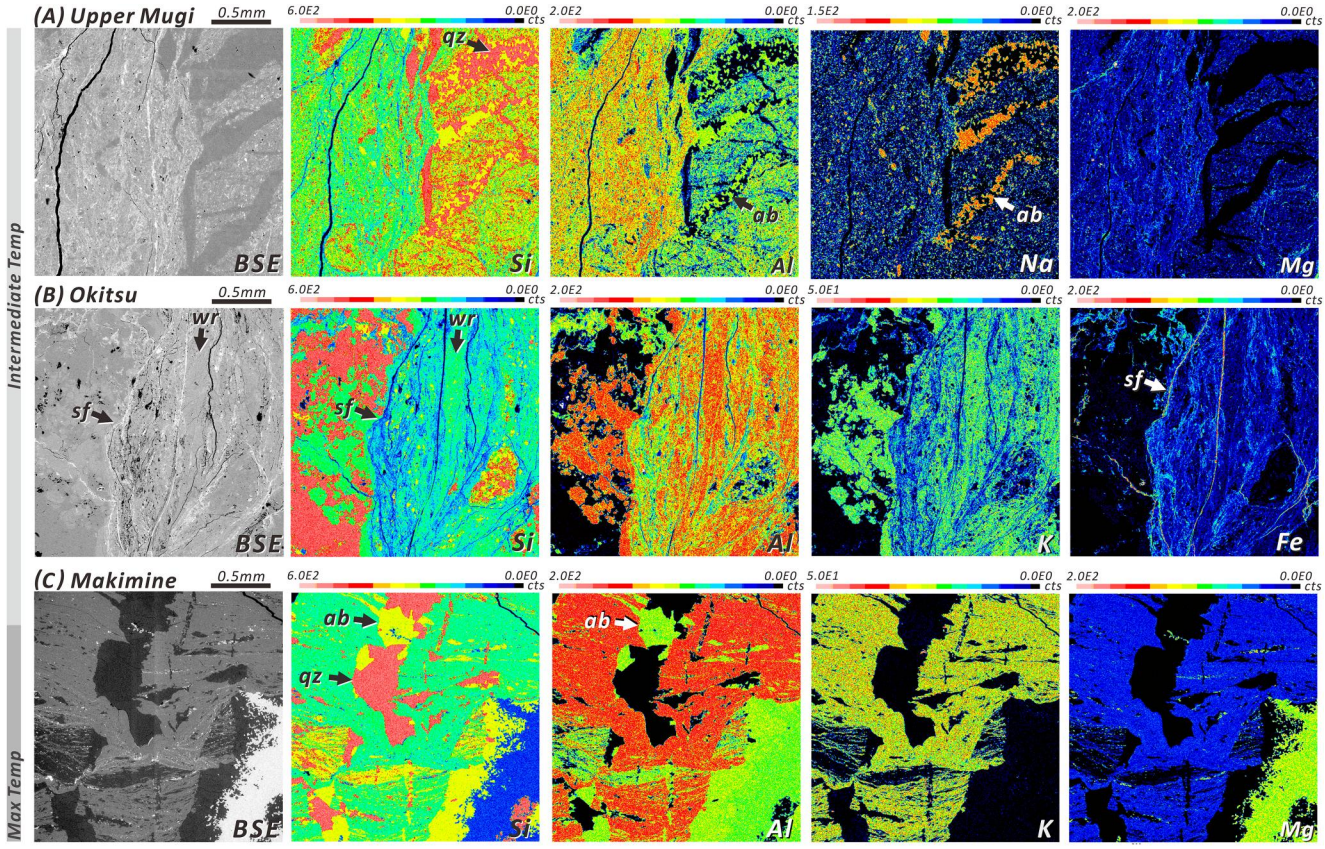

Figure 8. Element maps of Si, Al, K, Na, Mg, and Fe and backscattered electron (BSE) images for (a) the Upper Mugi, (b) Okitsu, and (c) Makimine mélanges, which record a gradual increase in paleotemperatures (Figure 3). The color bars in the maps represent counts per second (cts), which indicate the relative abundance of each element in the corresponding sample. Scaly fabrics (sf) appear as bright lines in BSE images and blue lines in Si, Al, and K maps due to the relative depletion of mobile elements compared to undeformed wall rocks (wr). These fabrics display as colorful lines in Mg and Fe maps resulting from the growth of phyllosilicates. The presence of albite (ab) and quartz (qz) in mineral veins is also revealed by the maps.

(Figure 8c). Na is also depleted along scaly fabrics and is only present in detrital grains of the undeformed mudstone phacoids, such as the orange grains on the Na map of the Upper Mugi mélange (Figure 8a and Figure S3 in Supporting Information S1). Combining the Na maps with the Si and Al maps reveals the presence of albite in the mineral veins, especially in the Upper Mugi and Makimine mélanges (Figures 8a and 8c), in addition to quartz, the major phase in the veins, which is shown as pink areas in the veins of Si maps (Figures 8 and 9a). In contrast, Fe and Mg are concentrated in the scaly fabrics, appearing as colorful lines on the maps (Figure 8, Figures S4 and S5 in Supporting Information S1); This is likely due to the growth of microscopic chlorite, as revealed by previous X-ray diffraction (XRD) analyses of the mélange units (Rajič et al., 2023; Ramirez et al., 2021).

5.2. Strain Calculation

5.2.1. Individual Volume Strain Along a Single Scaly Fabric

We used a broad spectrum of element concentrations, encompassing major, minor, and trace elements, in undeformed mudstone phacoids and scaly fabrics (Table S2) to assess the mass change of rocks during the alteration process based on the mass balance approach (e.g., Ague, 1991; Grant, 1986; Gresens, 1967). The approach assumes that the mass of a residual species *i* remains constant during the mass transfer process, leading to a change in the concentration of *i* as a result of the removal (resulting in an increase in the concentration of *i*) or addition (leading to a decrease in the concentration of *i*) of mobile species into the system. Thus, the total mass change of an altered rock can be calculated based on the reference species *i*, defined as T_i (Ague, 1991):

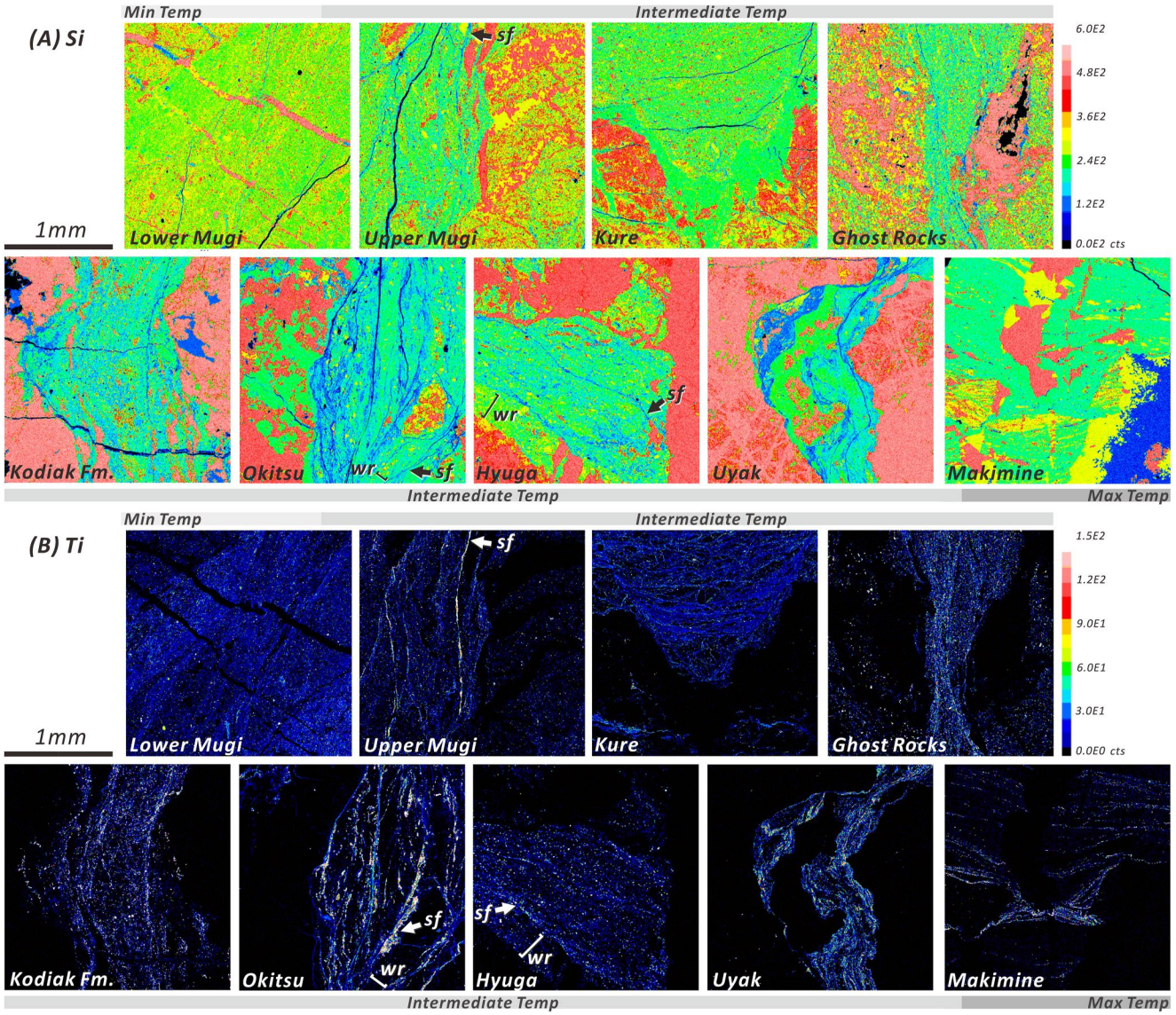

Figure 9. Element maps of (a) Si and (b) Ti for each mélange, arranged in order of increasing paleotemperature records (Figure 3) from the top left to the bottom right. Si depletion along scaly fabrics becomes more pronounced as the temperature records of the mélanges increase, resulting in increasing blue areas in the Si maps. Conversely, Ti enrichment along the fabrics become more prominent depicted as colorful lines in the Ti maps.

$$T_i = \frac{M^A - M^o}{M^O} = \frac{C_i^o}{C_i^A} - 1, \quad (1)$$

where C_i^o and C_i^A are the concentrations of species i in the original and altered rocks respectively, and M^o and M^A are the masses of the rocks before and after the alteration (Figure 10). To convert the mass change into the volume strain, denoted as ϵ_i, the density of original and altered rocks should be considered (Brimhall & Dietrich, 1987; Brimhall et al., 1988):

$$\epsilon_i = \frac{V^A - V^o}{V^O} = \frac{C_i^o}{C_i^A}\frac{\rho^o}{\rho^A} - 1, \quad (2)$$

where V^o and V^A are the volume of the rocks before and after the alteration, and ρ^o and ρ^A are the initial and final rock densities.

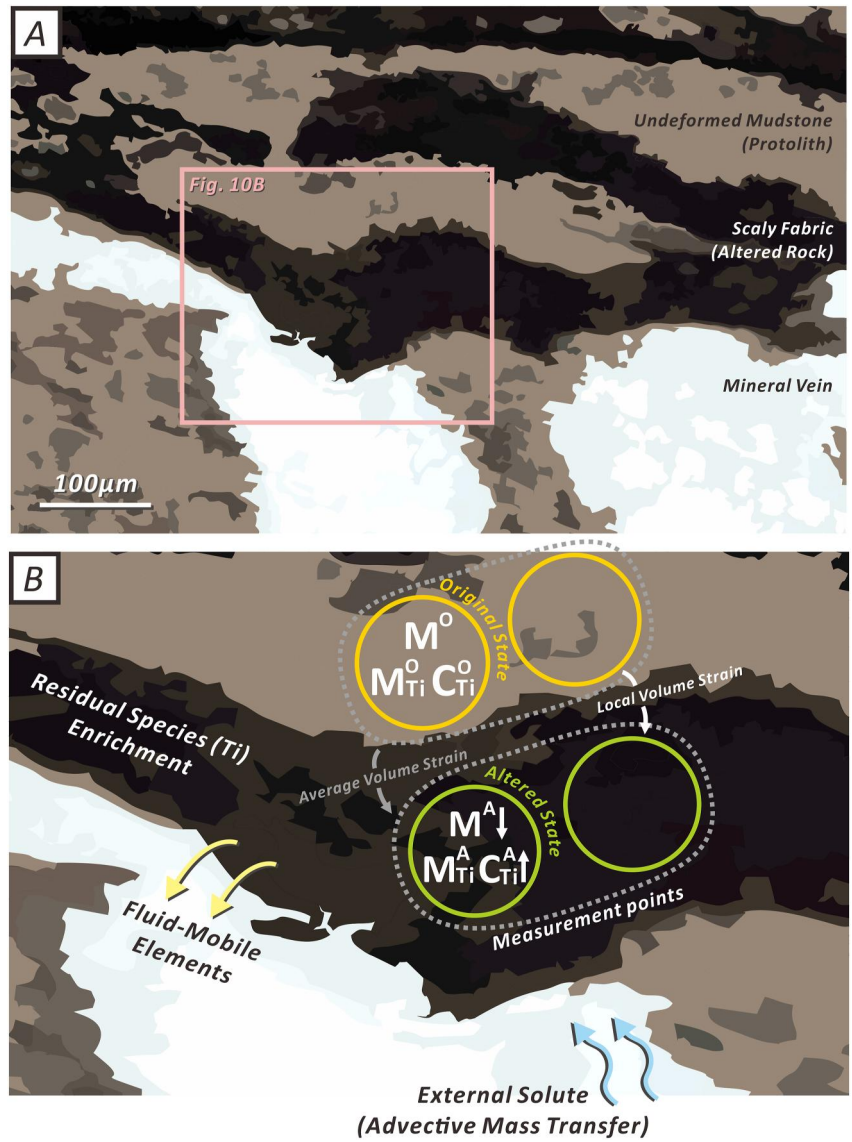

Figure 10. (a) Illustration depicting the phases present in the samples. (b) Schematic diagram of the mass balance approach. The mass of a residual species, such as Ti, remains constant in both original (M^{o}_{Ti}) and altered rocks (M^{A}_{Ti}), while the total mass of altered rocks (M^{A}) decreases due to the migration of mobile species, resulting in an increase in Ti concentration (C^{A}_{Ti}). A pair of yellow and green circles represent point measurements of Ti concentration in undeformed mudstones and adjacent scaly fabrics, respectively, which are used to determine a local volume strain at the corresponding spot. Average Ti concentrations in the two phases are determined by applying a statistical treatment to the data set and used to calculate the average volume loss in scaly fabrics. If the mass of vein materials exceeds the mass loss observed in scaly fabrics, it indicates the presence of an external supply via advection in addition to the local element redistribution though diffusion.

Here, we chose Ti as the conservative reference element due to its negative correlation with other mobile elements, such as Si, which has been observed in scaly fabrics of tectonic mélanges (Figure 9; Kawabata et al., 2007; Ramirez et al., 2021). Additionally, Ti is known to have limited mobility under various geological settings, as recognized in previous studies (e.g., Ague, 2017; Evans & Chester, 1995; Goddard & Evans, 1995; Tanaka et al., 2001). To determine the mass change of the rocks, we used each pair of point measurements of Ti concentration in undeformed mudstone and adjacent scaly fabrics as the parameters C^{o}_{i} and C^{A}_{i} (Figure 10). Using the assumption of applying average densities of quartz and illite for protoliths and scaly fabrics (i.e., ρ^{o} and ρ^{A}), we calculated the volume change for the corresponding spot on the individual scaly fabric. Analytical errors were propagated through the mass and volume change calculations using a series of Monte Carlo simulations.

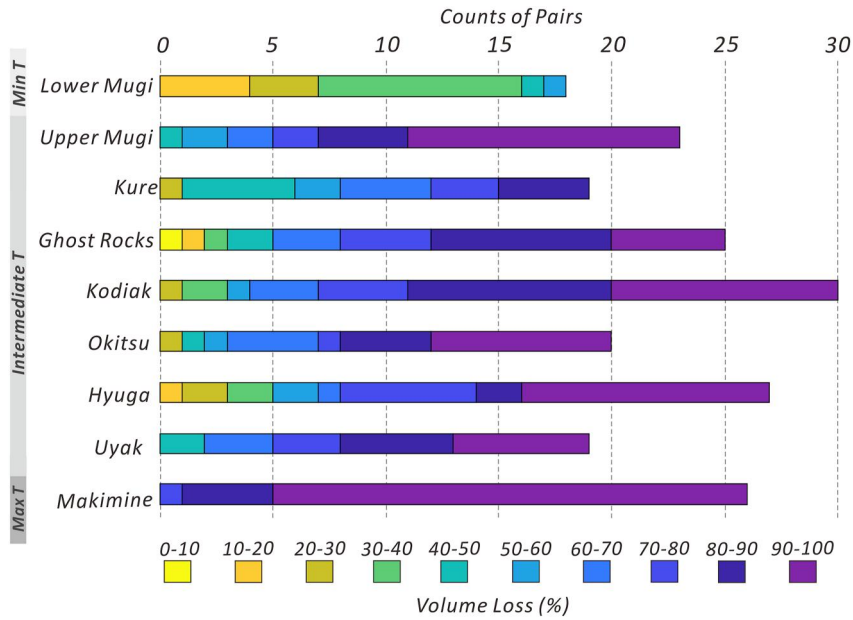

Figure 11. Stacked histogram showing the distribution of volume loss observed in individual scaly folia per mélange sample. The mélange units are arranged in order of increasing paleotemperature, as shown in Figure 3, from top to bottom.

The distribution of local volume loss in individual scaly fabrics for each sample is shown in Figure 11 and Table S3. A distinct difference was observed between the Lower Mugi and Makimine mélanges, which experienced temperatures near the updip and downdip isotherms bounding the seismogenic zone respectively. The Lower Mugi mélange exhibits individual scaly fabric volume loss ranging from 15% to 56%, while the Makimine mélange shows volume loss ranging from 72% to 99%. Other mélanges exposed to intermediate temperatures display a similar pattern, with a few points of volume loss below 50% and the majority experiencing volume loss greater than 50%.

5.2.2. Total Volume Strain in Each Mélange

Calculating average volume strain along a single scaly fabric on the basis of Ti for each mélange requires the average Ti concentrations in the heterogenous protoliths and altered mudstone (Figure 10). Here, we applied the statistic treatment of compositional data proposed by Ague (1994; Text S1 in Supporting Information S1), which also allows us to account for variations in the protolithology composition between different mélange units. The results show an average volume loss of 28% and 95% for the Lower Mugi and Makimine mélanges respectively. Other mélange units with intermediate temperatures yield volume losses between 63% and 88% (Figure 12a; Table S4).

To determine the total volume strain within areas of interest, we conducted image analyses on scanned images of the thin sections (Figure 7). We observed no temperature-dependency in the proportions of scaly fabrics, which ranged from 5% to 17% (Figure 12b; Table S4). Multiplying these values by the average volume loss in the scaly fabrics, we determined the total volumetric strain for each mélange (over the areas of thin sections), which ranges from 3% to 14%. We also observed no temperature-dependency in the total volumetric strain (Figure 12c). In addition, the observation of the veins serving as the sink for the redistributed elements (Figure 10; Ramirez et al., 2021) allowed us to correlate the proportion of veins with the amount of volume gain resulting from the mass transfer process. We determined the proportions of mineral veins in each thin section using the same image analysis techniques (Figure 7). The values estimated with image analysis ranged from 2% to 51% (Figure 12c; Table S4). We noted that the proportions of vein areas increased in mélange units with higher temperature records, such as the Hyuga, Uyak, and Makimine mélanges, leading to a higher discrepancy between the total volume loss and volume gain in these mélanges.

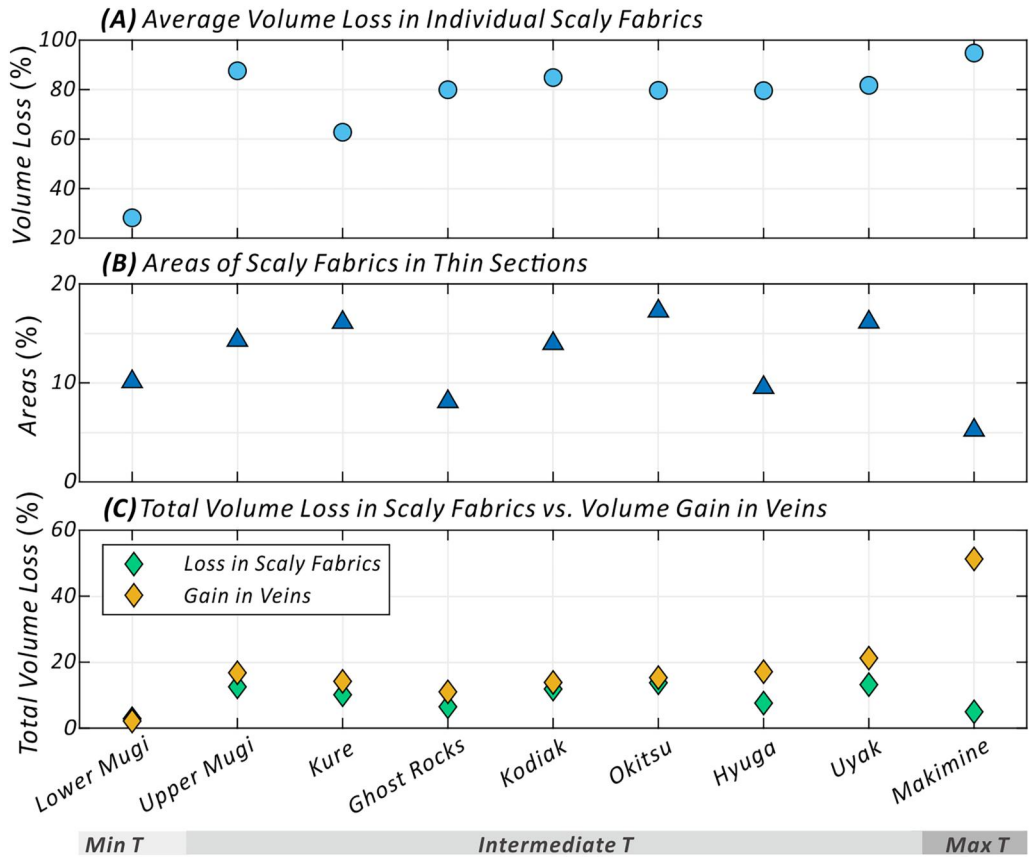

Figure 12. (a) The amount of average volume loss in individual scaly fabrics of each mélange. (b) The proportion of scaly fabrics in areas of each thin section determined by image analyses. (c) The comparison between the amount of total volume loss in scaly fabrics (green symbols) and the total volume gain in veins (orange symbols). Most uncertainties related to average and total volume loss are <1% (Table S4).

5.2.3. Average Mass Change of Each Element

Besides the bulk mass/volume change, we analyzed the average mass change of multiple elements in the scaly fabrics resulting from the mass transfer process using the method proposed by Ague (1991) in conjunction with the statistical treatment of Aitchison (1986) as documented in Ague (1994; Text S1 in Supporting Information S1). The results indicate a threshold between Sr and Y, with lighter elements having atomic numbers smaller than Y displaying higher mobility and greater mass loss. Ba, as an exception, behaves as a fluid-mobile element, which aligns with previous findings (e.g., Ishikawa et al., 2005; Sano et al., 2001). There is also a significant difference in the general mobility of elements between the Lower Mugi and Makimine mélange samples, consistent with the observed differences in bulk volume changes in scaly fabrics between the two units. In contrast, heavier elements with larger atomic numbers behave conservatively, with the elements in the Makimine mélange sample showing the highest immobility (Figure 13; Table S5). Moreover, we measured the element concentrations in quartz veins adjacent to the scaly fabrics. For elements with higher mobility such as Li, Al, and LILEs, there are higher corresponding concentrations detected in the veins. Conversely, HFSEs were not present in the veins, indicating their immobility (Figure 14; Table S6).

6. Discussion

6.1. Interseismic Deformation Along Plate Interfaces

Our study aims to investigate the relationship between temperature and diffusive mass transfer by examining the varying strain magnitudes along the depths of plate interfaces. This hypothesis is grounded in the temperature-dependent kinetics of the mechanism, suggesting that elevated temperatures likely facilitate more extensive

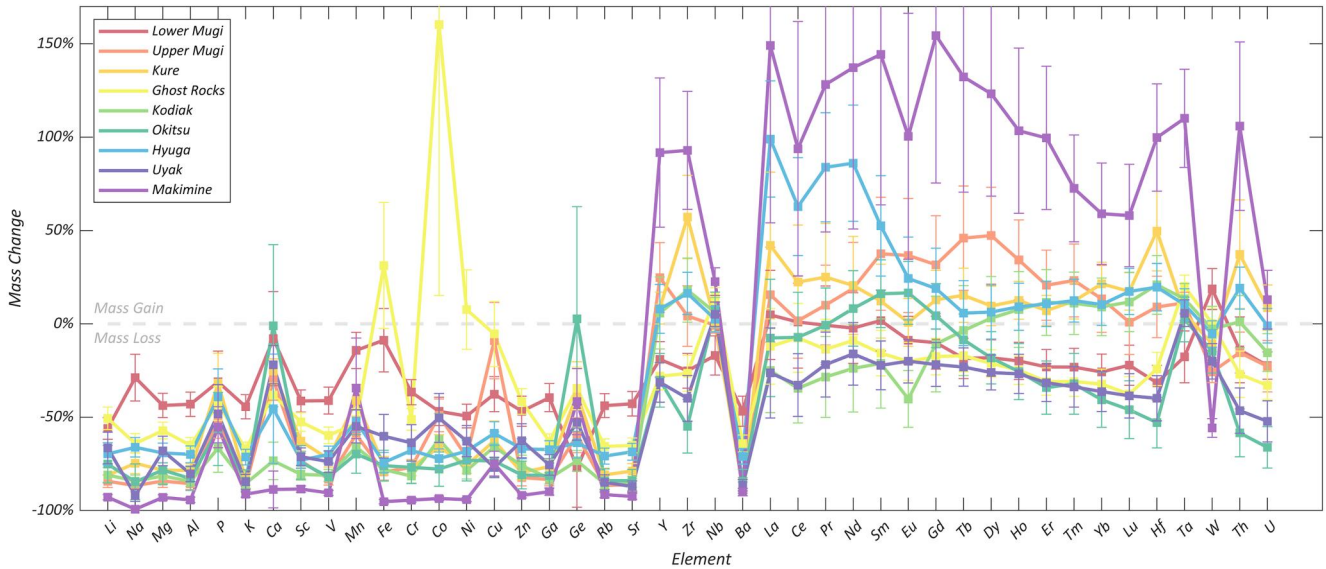

Figure 13. Average mass changes of various elements in scaly fabrics, with positive and negative values representing the gain and loss of mass during the mass transfer process, respectively.

deformation via mass transfer. Such enhanced deformation, in turn, accommodates a greater amount of plate motion, ultimately resulting in a reduced amount of coseismic slip or even a decreased potential for earthquake events. The initial validation of the hypothesis is evident in the pronounced depletion of fluid-mobile elements and the concurrent enrichment of fluid-immobile elements in scaly fabrics of mélanges with higher paleo-temperature records, as revealed by element maps (Figures 8 and 9). In addition, our quantification of the volumetric strain accumulated in a single scaly microfault reinforces this observation (Figures 11 and 12a).

While we maintained a consistent sampling criterion across each mélange by targeting outcrops with well-developed scaly fabrics, the limited number of samples incorporated in our analysis raises the possibility of not capturing the entire range of deformation levels within each unit. To mitigate potential bias, we collected data

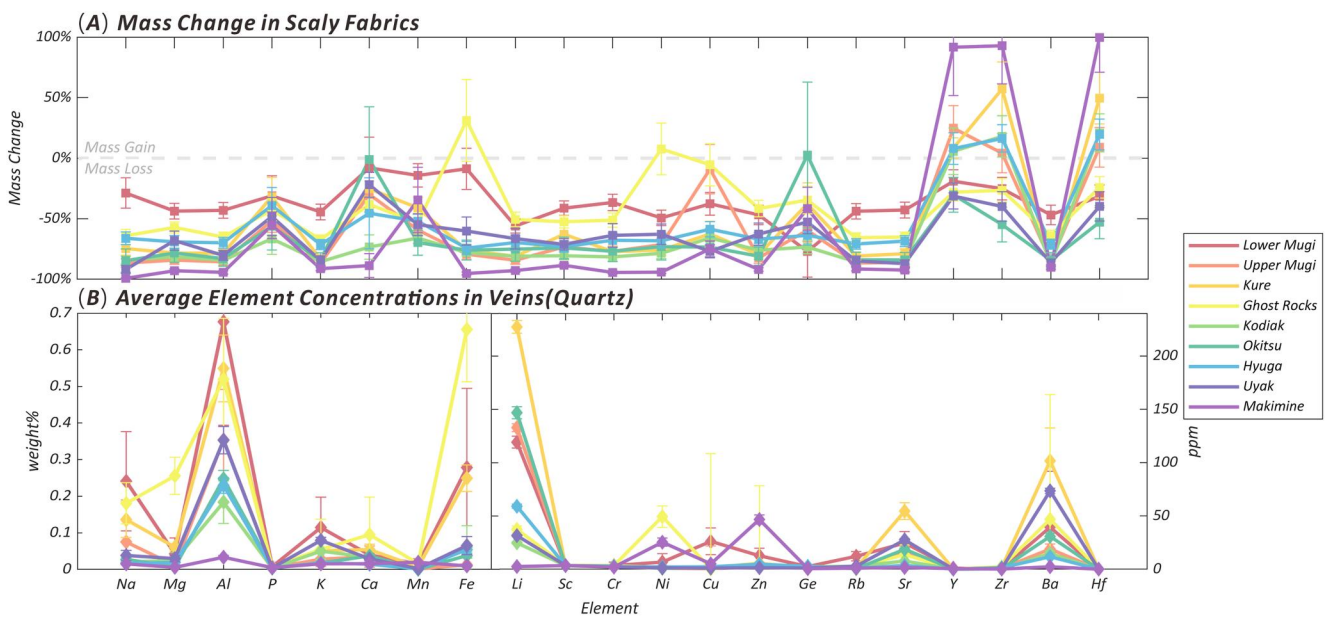

Figure 14. The comparison between (a) the average mass changes of various elements in scaly fabrics and (b) the presence of elements other than Si in quartz veins. The opposite patterns suggest that the elements dissolve along scaly fabrics and subsequently reprecipitate in the veins.

from various areas within a single thin section, aiming to encompass inherent variability. Taking the Upper Mugi mélange as an example, we analyzed element concentrations in four scaly fabrics and the adjacent protoliths. Mudstone protoliths exhibited consistent Ti concentrations ranging from 0.11% to 0.61%, while Ti concentrations in scaly fabrics varied significantly, spanning from 0.48% to 8.18% (Table S2). This diversity indicates that we encompassed a broad spectrum of deformation levels. To calculate the average volume loss in scaly fabrics, we applied robust statistical treatments (Text S1 in Supporting Information S1) on this highly variable data set. Implicit in our approach is the assumption that the microscale variation we addressed is reflective of the broader heterogeneity observable at larger scales. Furthermore, the temperature-dependent strain we observed in scaly fabrics is considered indicative of the broader conditions within these subduction mélanges.

Another critical factor affecting the estimation of total volumetric strain is the density of scaly fabrics, which is not strictly tied to temperature. For subduction mélanges to undergo the requisite amount of shearing leading to temperature-dependent changes in scaly fabric density, they must consistently remain in proximity to the décollement throughout their subduction paths. Although we observed higher strain in individual scaly fabrics under elevated temperatures, the intensity of scaly microfaults may be lower due to the shorter duration during which the mélanges were underthrusted before being underplated. This may explain why we did not observe any temperature-dependency for the integrated volumetric strain recorded in the mélange units (Figure 12c).

Another possibility is that our integration of strain over thin section areas may not be representative of the mélanges due to the large scale and heterogeneity of the deformation. For instance, the density of scaly fabric was measured at 14.3% in our Upper Mugi thin section, while Kawabata et al. (2007) determined scaly fabric densities in five thin sections from the same mélange, ranging from 32.9% to 48.8%. Combining the average volume change of −87.6% in individual scaly fabrics estimated in our study with these density values, the total volume change could span a wide range from −12.5% to −42.8%. This underscores the need for a more extensive characterization at a larger scale to accurately determine this parameter. Given that our study encompasses nine mélange units across two accretionary complexes, achieving detailed characterizations for all mélange units within the scope of a single study is challenging. Nonetheless, we demonstrate the validity of quantifying strain within individual microstructures and show that the method can be seamlessly integrated with different scales of characterization, allowing for strain quantification at the thin section scale, outcrop scale, and even regional scale.

Although there are limitations to our study, our results offer an initial estimate of the strain rate associated with the mass transfer process. Here, we use the Uyak and Makimine mélanges as examples. Assuming an average slab-top geotherm of 11°C/km (England & Smye, 2023) and a median plate motion rate of 5 cm/yr, we estimate that it would require 0.25 and 0.35 m.y. to subduct the Uyak mélange from 150°C down to 290°C and the Makimine mélange from 150°C to 340°C based on their maximum burial temperature records (Figure 3). The least principle stretch of the two mélanges after the deformation is 0.87 and 0.95 based on our calculation of the 13% and 5% of total volume loss. Dividing the strain by the time durations, we obtain strain rates of 1.1×10^{-13} and 8.6×10^{-14} s^{-1} for the two mélange units, respectively.

Assuming a general width of 100 m for the plate boundary fault zone (e.g., Rowe et al., 2013), a strain rate of 10^{-11} s^{-1} is required to fully accommodate the plate motion of 5 cm/yr at the base of the seismogenic zone, which is several orders of magnitude higher than our estimation. However, shear zones involving a volume change, such as subduction fault zones, require two components to describe them: the simple shear component (γ) and the volume change component (Δ, Ramsay, 1980). In this study, we focus on estimating the second component and present a method to quantify volumetric strain related to a specific microstructure. Our method can be further applied to scaly microfaults where the amount of slip can be measured through microstructural analysis, allowing for the quantification of both components of deformation. This enables a more comprehensive assessment of the hypothesis that the mass transfer process affects the accumulation of slip deficit by accommodating significant strain.

6.2. Fluid-Rock Interaction in Subduction Fault Zones

Diffusive mass transfer is a fluid-assisted mechanism, and therefore, the associated strain magnitude observed in the mélanges can provide insights into the amount of fluid that has interacted with the rocks along plate interfaces. The significant losses of Si, Al, K, and Na observed in scaly fabrics (Figures 8 and 13), and the high clay mineral content revealed by previous XRD analysis of the mélange units (Rajič et al., 2023; Ramirez et al., 2021) suggest that the transformation of mudstones involves the breakdown of quartz and feldspars and the formation of

phyllosilicates. The reactions involved in this process likely include the dissolution and metamorphic reactions, such as:

quartz to dissolved silica:

$$SiO_2 + H_2O \rightarrow H_4SiO_4 \quad (3)$$

albite to illite:

$$5NaAlSi_3O_8 + 4H^+ \rightarrow NaAl_4Si_7AlO_{20}(OH)_4 + 4Na^+ + 8SiO_2 \quad (4)$$

albite to kaolinite:

$$2NaAlSi_3O_8 + 9H_2O + 2H^+ \rightarrow Al_4Si_4O_{10}(OH)_8 + 2Na^+ + 8H_4SiO_4 \quad (5)$$

as proposed by Beach (1979) and Goddard and Evans (1995). These reactions involve water or H^+ ions and result in the liberation of SiO_2.

Raimbourg et al. (2015) revealed two distinct types of quartz in veins of the Hyuga mélange: one originating from "local" fluid sources, likely tied to dehydration or metamorphic reactions, and the other linked to "external" fluid sources resulting from post-seismic fluid circulation. This observation aligns with our finding of a significant discrepancy between the volume gain in mineral veins and the volume loss in scaly fabrics within the Makimine mélange (Figure 12c). Besides the locally redistributed materials that diffused from scaly fabrics at a microscale with the assistance of nearby fluids, there appears to be an additional source contributing to the material within the veins through long-distance transport, potentially extending up to kilometer-scale distances (Figure 10).

At the top of the seismogenic zone where the Lower Mugi mélange has subducted to, the primary fluid sources are water expelled from the pore spaces of subducted sediments by compaction and water released by the smectite-to-illite transition (e.g., Saffer et al., 2008). Post-seismic fluid circulation likely involves the percolation of seawater from shallower depths as the "external" fluid source, facilitating the transport of solute over kilometer-scale distances (Raimbourg et al., 2015). For the Makimine mélange, which has subducted to the base of the seismogenic zone, these fluid sources are absent. Fisher et al. (2021) employed a numerical model developed by Hooker and Fisher (2021), which considered the negative feedback between the dissolution-precipitation process and permeability along plate interfaces and demonstrated a post-seismic updip migration of fluid due to the rupture of seals resulting from the diffusive mass transfer process. This allows the fluid generated by the dehydration of subducted oceanic crusts at depth to transport upward, which likely explains the large amount of external fluid required for the additional deposition of veins observed in our analysis.

7. Conclusions

We conducted micro-chemical analysis on a suite of subduction mélanges that experienced peak temperatures relevant to the seismogenic zone of active convergent margins. Our analysis using EPMA produced element maps that reveal an amplification in depletion of fluid-mobile elements and enrichment of fluid-immobile elements along scaly fabrics in mélanges with higher paleotemperature records. This indicates an enhanced level of diffusive mass transfer at greater depths of subduction interfaces. To quantify the strain related to the dissolution-precipitation process, we applied chemical mass-balance analysis. We observed a 67% difference in average volume loss in individual scaly fabrics of Lower Mugi and Makimine mélanges, which were subducted to the top and base of the seismogenic zone, respectively. We then used image analysis to determine the proportion of scaly fabrics in the areas of interest and integrated the strain over those areas. However, the spatially-integrated volume loss did not exhibit temperature dependence, which suggests that larger scales of characterization may be required or that the mélange units did not remain underthrusted during subduction. The volume gain was represented by the percentage of mineral veins, which served as the sink for the redistributed elements from scaly fabrics based on the opposite pattern of element distribution we observed. The discrepancy between the total volume loss and the volume gain in the Makimine mélange suggested the existence of an external fluid source that likely originated from a greater depth.

Data Availability Statement

The LA-ICPMS, strain calculations, and image analysis data presented in this paper are available at Zenodo via (Chen et al., 2023) https://doi.org/10.5281/zenodo.7948891 with open access.

Acknowledgments
This research was supported by the National Science Foundations (NSF) Award EAR-1524530 and EAR-2214324 from the Tectonics Program awarded to D. Fisher. T.-W. Chen would like to thank J. Cipar for the guidance of the image processing method, K. Crispin and M. Feineman for the technical support of EPMA data collection, and J. Garber for the LA-ICPMS and Axioscan data collection and comments on the method description. Finally, we express our appreciation to R. Williams and an anonymous reviewer for their constructive feedback, which greatly contributed to the enhancement of this manuscript. We also extend our gratitude to the editor, W. Behr, for managing the review process.

References

Abràmoff, M. D., Magalhães, P. J., & Ram, S. J. (2004). Image processing with ImageJ. *Biophotonics International*, *11*(7), 36–42.
Ague, J. J. (1991). Evidence for major mass transfer and volume strain during regional metamorphism of pelites. *Geology*, *19*(8), 855–858. https://doi.org/10.1130/0091-7613(1991)019<0855:EFMMTA>2.3.CO;2
Ague, J. J. (1994). Mass transfer during Barrovian metamorphism of pelites, south-central Connecticut; I, Evidence for changes in composition and volume. *American Journal of Science*, *294*(8), 989–1057. https://doi.org/10.2475/ajs.294.8.989
Ague, J. J. (2017). Element mobility during regional metamorphism in crustal and subduction zone environments with a focus on the rare earth elements (REE). *American Mineralogist: Journal of Earth and Planetary Materials*, *102*(9), 1796–1821. https://doi.org/10.2138/am-2017-6130
Aitchison, J. (1986). *The statistical analysis of compositional data*. Chapman and Hall.
Beach, A. (1979). Pressure solution as a metamorphic process in deformed terrigenous sedimentary rocks. *Lithos*, *12*(1), 51–58. https://doi.org/10.1016/0024-4937(79)90062-8
Brimhall, G. H., & Dietrich, W. E. (1987). Constitutive mass balance relations between chemical composition, volume, density, porosity, and strain in metasomatic hydrochemical systems: Results on weathering and pedogenesis. *Geochimica et Cosmochimica Acta*, *51*(3), 567–587. https://doi.org/10.1016/0016-7037(87)90070-6
Brimhall, G. H., Lewis, C. J., Ague, J. J., Dietrich, W. E., Hampel, J., Teague, T., & Rix, P. (1988). Metal enrichment in bauxites by deposition of chemically mature aeolian dust. *Nature*, *333*(6176), 819–824. https://doi.org/10.1038/333819a0
Byrne, T. (1982). Structural evolution of coherent terranes in the Ghost Rocks Formation, Kodiak Island, Alaska. *Geological Society, London, Special Publications*, *10*(1), 229–242. https://doi.org/10.1144/GSL.SP.1982.010.01.15
Byrne, T. (1984). Early deformation in mélange terranes of the Ghost Rocks Formation, Kodiak islands, Alaska. *Melanges: Their nature, origin, and significance*, *198*, 21–52. https://doi.org/10.1130/SPE198-p21
Byrne, T., & Fisher, D. (1990). Evidence for a weak and overpressured decollement beneath sediment-dominated accretionary prisms. *Journal of Geophysical Research*, *95*(B6), 9081–9097. https://doi.org/10.1029/JB095iB06p09081
Chen, T., Smye, A., Fisher, D., Hashimoto, Y., Raimbourg, H., & Famin, V. (2023). Quantifying interseismic volume strain from chemical mass-balance analysis in tectonic mélanges [Dataset]. Zenodo. https://doi.org/10.5281/zenodo.7948891
Connelly, W. (1978). Uyak complex, Kodiak islands, Alaska: A cretaceous subduction complex. *Geological Society of America Bulletin*, *89*(5), 755–769. https://doi.org/10.1130/0016-7606(1978)89<755:UCKIAA>2.0.CO;2
England, P. C., & Smye, A. J. (2023). Metamorphism and deformation on subduction interfaces: 1. Physical framework. *Geochemistry, Geophysics, Geosystems*, *24*(1), e2022GC010644. https://doi.org/10.1029/2022GC010644
Evans, J. P., & Chester, F. M. (1995). Fluid-rock interaction in faults of the San Andreas system: Inferences from San Gabriel fault rock geochemistry and microstructures. *Journal of Geophysical Research*, *100*(B7), 13007–13020. https://doi.org/10.1029/94JB02625
Fisher, D., & Byrne, T. (1987). Structural evolution of underthrusted sediments, Kodiak Islands, Alaska. *Tectonics*, *6*(6), 775–793. https://doi.org/10.1029/TC006i006p00775
Fisher, D. M., & Brantley, S. L. (2014). The role of silica redistribution in the evolution of slip instabilities along subduction interfaces: Constraints from the Kodiak accretionary complex, Alaska. *Journal of Structural Geology*, *69*, 395–414. https://doi.org/10.1016/j.jsg.2014.03.010
Fisher, D. M., Hooker, J. N., Smye, A. J., & Chen, T. W. (2021). Insights from the geological record of deformation along the subduction interface at depths of seismogenesis. *Geosphere*, *17*(6), 1686–1703. https://doi.org/10.1130/GES02389.1
Fisher, D. M., Smye, A. J., Marone, C., Van Keken, P. E., & Yamaguchi, A. (2019). Kinetic models for healing of the subduction interface based on observations of ancient accretionary complexes. *Geochemistry, Geophysics, Geosystems*, *20*(7), 3431–3449. https://doi.org/10.1029/2019GC008256
Goddard, J. V., & Evans, J. P. (1995). Chemical changes and fluid-rock interaction in faults of crystalline thrust sheets, northwestern Wyoming, USA. *Journal of Structural Geology*, *17*(4), 533–547. https://doi.org/10.1016/0191-8141(94)00068-B
Grant, J. A. (1986). The isocon diagram; a simple solution to Gresens' equation for metasomatic alteration. *Economic Geology*, *81*(8), 1976–1982. https://doi.org/10.2113/gsecongeo.81.8.1976
Gratier, J. P., Favreau, P., & Renard, F. (2003). Modeling fluid transfer along California faults when integrating pressure solution crack sealing and compaction processes. *Journal of Geophysical Research*, *108*(B2), 2104. https://doi.org/10.1029/2001JB000380
Gresens, R. L. (1967). Composition-volume relationships of metasomatism. *Chemical Geology*, *2*, 47–65. https://doi.org/10.1016/0009-2541(67)90004-6
Gutscher, M. A., & Peacock, S. M. (2003). Thermal models of flat subduction and the rupture zone of great subduction earthquakes. *Journal of Geophysical Research*, *108*(B1). ESE-2. https://doi.org/10.1029/2001JB000787
Hara, H., & Kimura, K. (2008). Metamorphic and cooling history of the Shimanto accretionary complex, Kyushu, Southwest Japan: Implications for the timing of out-of-sequence thrusting. *Island Arc*, *17*(4), 546–559. https://doi.org/10.1111/j.1440-1738.2008.00636.x
Hashimoto, Y., Eida, M., Kirikawa, T., Iida, R., Takagi, M., Furuya, N., et al. (2012). Large amount of fluid migration around shallow seismogenic depth preserved in tectonic mélange: Yokonami mélange, the Cretaceous Shimanto Belt, Kochi, Southwest Japan. *Island Arc*, *21*(1), 53–64. https://doi.org/10.1111/j.1440-1738.2011.00806.x
Hashimoto, Y., Enjoji, M., Sakaguchi, A., & Kimura, G. (2002). PT conditions of cataclastic deformation associated with underplating: An example from the Cretaceous Shimanto complex, Kii Peninsula, SW Japan. *Earth Planets and Space*, *54*(11), 1133–1138. https://doi.org/10.1186/BF03353314
Hashimoto, Y., Enjoji, M., Sakaguchi, A., & Kimura, G. (2003). In situ pressure–temperature conditions of a tectonic mélange: Constraints from fluid inclusion analysis of syn-mélange veins. *Island Arc*, *12*(4), 357–365. https://doi.org/10.1046/j.1440-1738.2003.00405.x
Hashimoto, Y., & Kimura, G. (1999). Underplating process from melange formation to duplexing: Example from the cretaceous Shimanto belt, Kii Peninsula, southwest Japan. *Tectonics*, *18*(1), 92–107. https://doi.org/10.1029/1998TC900014
Hooker, J. N., & Fisher, D. M. (2021). How cementation and fluid flow influence slip behavior at the subduction interface. *Geology*, *49*(9), 1074–1078. https://doi.org/10.1130/G48741.1

Hyndman, R. D., & Wang, K. (1993). Thermal constraints on the zone of major thrust earthquake failure: The Cascadia subduction zone. *Journal of Geophysical Research*, *98*(B2), 2039–2060. https://doi.org/10.1029/92JB02279

Hyndman, R. D., Yamano, M., & Oleskevich, D. A. (1997). The seismogenic zone of subduction thrust faults. *Island Arc*, *6*(3), 244–260. https://doi.org/10.1111/j.1440-1738.1997.tb00175.x

Ikesawa, E., Kimura, G., Sato, K., Ikehara-Ohmori, K., Kitamura, Y., Yamaguchi, A., et al. (2005). Tectonic incorporation of the upper part of oceanic crust to overriding plate of a convergent margin: An example from the Cretaceous–early Tertiary Mugi Mélange, the Shimanto Belt, Japan. *Tectonophysics*, *401*(3–4), 217–230. https://doi.org/10.1016/j.tecto.2005.01.005

Ikesawa, E., Sakaguchi, A., & Kimura, G. (2003). Pseudotachylyte from an ancient accretionary complex: Evidence for melt generation during seismic slip along a master décollement? *Geology*, *31*(7), 637–640. https://doi.org/10.1130/0091-7613(2003)031<0637:PFAAAC>2.0.CO;2

Ishikawa, T., Fujisawa, S., Nagaishi, K., & Masuda, T. (2005). Trace element characteristics of the fluid liberated from amphibolite-facies slab: Inference from the metamorphic sole beneath the Oman ophiolite and implication for boninite genesis. *Earth and Planetary Science Letters*, *240*(2), 355–377. https://doi.org/10.1016/j.epsl.2005.09.049

Jochum, K. P., Dingwell, D. B., Rocholl, A., Stoll, B., Hofmann, A. W., Becker, S., et al. (2000). The preparation and preliminary characterisation of eight geological MPI-DING reference glasses for in-situ microanalysis. *Geostandards Newsletter*, *24*(1), 87–133. https://doi.org/10.1111/j.1751-908X.2000.tb00590.x

Kawabata, K., Tanaka, H., & Kimura, G. (2007). Mass transfer and pressure solution in deformed shale of accretionary complex: Examples from the Shimanto Belt, southwestern Japan. *Journal of Structural Geology*, *29*(4), 697–711. https://doi.org/10.1016/j.jsg.2006.11.009

Kiminami, K., & Ohno, Y. (1999). Vitrinite reflectance and contact metamorphism on argillites by basaltic rocks in an accretionary complex: An example from the Late Cretaceous Makimine Formation, Kyushu. *Memoirs of the Geological Society of Japan*, *52*, 243–253. (in Japanese with English Abstract).

Kimura, G., & Mukai, A. (1991). Underplated units in an accretionary complex: Melange of the Shimanto Belt of eastern Shikoku, southwest Japan. *Tectonics*, *10*(1), 31–50. https://doi.org/10.1029/90TC00799

Kimura, G., Yamaguchi, A., Hojo, M., Kitamura, Y., Kameda, J., Ujiie, K., et al. (2012). Tectonic mélange as fault rock of subduction plate boundary. *Tectonophysics*, *568*, 25–38. https://doi.org/10.1016/j.tecto.2011.08.025

Kitamura, Y., & Kimura, G. (2012). Dynamic role of tectonic mélange during interseismic process of plate boundary mega earthquakes. *Tectonophysics*, *568*, 39–52. https://doi.org/10.1016/j.tecto.2011.07.008

Kitamura, Y., Sato, K., Ikesawa, E., Ikehara-Ohmori, K., Kimura, G., Kondo, H., et al. (2005). Mélange and its seismogenic roof décollement: A plate boundary fault rock in the subduction zone—An example from the Shimanto belt, Japan. *Tectonics*, *24*(5), TC5012. https://doi.org/10.1029/2004TC001635

Kondo, H., Kimura, G., Masago, H., Ohmori-Ikehara, K., Kitamura, Y., Ikesawa, E., et al. (2005). Deformation and fluid flow of a major out-of-sequence thrust located at seismogenic depth in an accretionary complex: Nobeoka Thrust in the Shimanto Belt, Kyushu, Japan. *Tectonics*, *24*(6), TC6008. https://doi.org/10.1029/2004TC001655

Matsumura, M., Hashimoto, Y., Kimura, G., Ohmori-Ikehara, K., Enjohji, M., & Ikesawa, E. (2003). Depth of oceanic-crust underplating in a subduction zone: Inferences from fluid-inclusion analyses of crack-seal veins. *Geology*, *31*(11), 1005–1008. https://doi.org/10.1130/G19885.1

Meneghini, F., Di Toro, G., Rowe, C. D., Moore, J. C., Tsutsumi, A., & Yamaguchi, A. (2010). Record of mega-earthquakes in subduction thrusts: The black fault rocks of Pasagshak Point (Kodiak Island, Alaska). *Bulletin*, *122*(7–8), 1280–1297. https://doi.org/10.1130/B30049.1

Moore, J. C., Byrne, T., Plumley, P. W., Reid, M., Gibbons, H., & Coe, R. S. (1983). Paleogene evolution of the Kodiak Islands, Alaska: Consequences of ridge-trench interaction in a more southerly latitude. *Tectonics*, *2*(3), 265–293. https://doi.org/10.1029/TC002i003p00265

Mukoyoshi, H., Hirono, T., Hara, H., Sekine, K., Tsuchiya, N., Sakaguchi, A., & Soh, W. (2009). Style of fluid flow and deformation in and around an ancient out-of-sequence thrust: An example from the Nobeoka Tectonic Line in the Shimanto accretionary complex, Southwest Japan. *Island Arc*, *18*(2), 333–351. https://doi.org/10.1111/j.1440-1738.2009.00670.x

Mukoyoshi, H., Sakaguchi, A., Otsuki, K., Hirono, T., & Soh, W. (2006). Co-seismic frictional melting along an out-of-sequence thrust in the Shimanto accretionary complex. Implications on the tsunamigenic potential of splay faults in modern subduction zones. *Earth and Planetary Science Letters*, *245*(1–2), 330–343. https://doi.org/10.1016/j.epsl.2006.02.039

Myers, G., & Vrolijk, P. J. (1986). Fluid evolution associated with the accretion of the Kodiak Formation, Kodiak Island, Alaska. *Eos Trans. AGU*, *67*, 1219.

Oleskevich, D. A., Hyndman, R. D., & Wang, K. (1999). The updip and downdip limits to great subduction earthquakes: Thermal and structural models of Cascadia, south Alaska, SW Japan, and Chile. *Journal of Geophysical Research*, *104*(B7), 14965–14991. https://doi.org/10.1029/1999JB900060

Onishi, C. T., & Kimura, G. (1995). Change in fabric of mélange in the Shimanto Belt, Japan: Change in relative convergence? *Tectonics*, *14*(6), 1273–1289. https://doi.org/10.1029/95TC01929

Paton, C., Hellstrom, J., Paul, B., Woodhead, J., & Hergt, J. (2011). Iolite: Freeware for the visualisation and processing of mass spectrometric data. *Journal of Analytical Atomic Spectrometry*, *26*(12), 2508–2518. https://doi.org/10.1039/C1JA10172B

Raimbourg, H., Famin, V., Palazzin, G., Yamaguchi, A., & Augier, R. (2017). Tertiary evolution of the Shimanto belt (Japan): A large-scale collision in early Miocene. *Tectonics*, *36*(7), 1317–1337. https://doi.org/10.1002/2017TC004529

Raimbourg, H., Famin, V., Palazzin, G., Yamaguchi, A., Augier, R., Kitamura, Y., & Sakaguchi, A. (2019). Distributed deformation along the subduction plate interface: The role of tectonic mélanges. *Lithos*, *334*, 69–87. https://doi.org/10.1016/j.lithos.2019.01.033

Raimbourg, H., Rajič, K., Moris-Muttoni, B., Famin, V., Palazzin, G., Fisher, D., et al. (2021). Quartz vein geochemistry records deformation processes in convergent zones. *Geochemistry, Geophysics, Geosystems*, *22*(4), e2020GC009201. https://doi.org/10.1029/2020GC009201

Raimbourg, H., Vacelet, M., Ramboz, C., Famin, V., Augier, R., Palazzin, G., et al. (2015). Fluid circulation in the depths of accretionary prisms: An example of the Shimanto belt, Kyushu, Japan. *Tectonophysics*, *655*, 161–176. https://doi.org/10.1016/j.tecto.2015.05.023

Rajič, K., Raimbourg, H., Lerouge, C., Famin, V., Dubacq, B., Canizarés, A., et al. (2023). Metamorphic reactions and their implication for the fluid budget in metapelites at seismogenic depths in subduction zones. *Tectonophysics*, *857*, 229844. https://doi.org/10.1016/j.tecto.2023.229844

Ramirez, G., Smye, A., Fisher, D. M., Hashimoto, Y., & Yamaguchi, A. (2021). Constraints on element mobility during deformation within the seismogenic zone, Shimanto belt, Japan. *Geochemistry, Geophysics, Geosystems*, *22*(8), e2020GC009594. https://doi.org/10.1029/2020GC009594

Ramsay, J. (1980). Shear zone geometry: A review. *Journal of Structural Geology*, *2*(1–2), 83–99. https://doi.org/10.1016/0191-8141(80)90038-3

Rowe, C. D., Meneghini, F., & Moore, J. C. (2009). Fluid-rich damage zone of an ancient out-of-sequence thrust, Kodiak Islands, Alaska. *Tectonics*, *28*(1), TC1006. https://doi.org/10.1029/2007TC002126

Rowe, C. D., Moore, J. C., & Remitti, F., & IODP Expedition 343/343T Scientists. (2013). The thickness of subduction plate boundary faults from the seafloor into the seismogenic zone. *Geology*, *41*(9), 991–994. https://doi.org/10.1130/G34556.1

Saffer, D. M., Underwood, M. B., & McKiernan, A. W. (2008). Evaluation of factors controlling smectite transformation and fluid production in subduction zones: Application to the Nankai Trough. *Island Arc*, *17*(2), 208–230. https://doi.org/10.1111/j.1440-1738.2008.00614.x

Sakaguchi, A. (1996). High paleogeothermal gradient with ridge subduction beneath the Cretaceous Shimanto accretionary prism, southwest Japan. *Geology*, *24*(9), 795–798. https://doi.org/10.1130/0091-7613(1996)024<0795:HPGWRS>2.3.CO;2

Sample, J. C., & Moore, J. C. (1987). Structural style and kinematics of an underplated slate belt, Kodiak and adjacent islands, Alaska. *Geological Society of America Bulletin*, *99*(1), 7–20. https://doi.org/10.1130/0016-7606(1987)99<7:SSAKOA>2.0.CO;2

Sano, T., Hasenaka, T., Shimaoka, A., Yonezawa, C., & Fukuoka, T. (2001). Boron contents of Japan trench sediments and Iwate basaltic lavas, northeast Japan arc: Estimation of sediment-derived fluid contribution in mantle wedge. *Earth and Planetary Science Letters*, *186*(2), 187–198. https://doi.org/10.1016/S0012-821X(01)00244-8

Taira, A. (1980). The geology of the Shimanto belt in Kochi Prefecture, Shikoku, Japan. *Geology and paleontology of the Shimanto Belt*, 319–389.

Taira, A., Katto, J., Tashiro, M., Okamura, M., & Kodama, K. (1988). The Shimanto belt in Shikoku, Japan.-Evolution of Cretaceous to Miocene accretionary prism. *Modern Geology*, *12*, 5–46.

Tanaka, H., Fujimoto, K., Ohtani, T., & Ito, H. (2001). Structural and chemical characterization of shear zones in the freshly activated Nojima fault, Awaji Island, southwest Japan. *Journal of Geophysical Research*, *106*(B5), 8789–8810. https://doi.org/10.1029/2000JB900444

Ujiie, K. (1997). Off-scraping accretionary process under the subduction of young oceanic crust: The Shimanto Belt of Okinawa Island, Ryukyu Arc. *Tectonics*, *16*(2), 305–322. https://doi.org/10.1029/96TC03367

Ujiie, K. (2002). Evolution and kinematics of an ancient décollement zone, mélange in the Shimanto accretionary complex of Okinawa Island, Ryukyu Arc. *Journal of Structural Geology*, *24*(5), 937–952. https://doi.org/10.1016/S0191-8141(01)00103-1

Ujiie, K., Saishu, H., Fagereng, Å., Nishiyama, N., Otsubo, M., Masuyama, H., & Kagi, H. (2018). An explanation of episodic tremor and slow slip constrained by crack-seal veins and viscous shear in subduction mélange. *Geophysical Research Letters*, *45*(11), 5371–5379. https://doi.org/10.1029/2018gl078374

Vrolijk, P., Myers, G., & Moore, J. C. (1988). Warm fluid migration along tectonic melanges in the Kodiak accretionary complex, Alaska. *Journal of Geophysical Research*, *93*(B9), 10313–10324. https://doi.org/10.1029/JB093iB09p10313

Williams, R. T., & Fagereng, Å. (2022). The role of quartz cementation in the seismic cycle: A critical review. *Reviews of Geophysics*, *60*(1), e2021RG000768. https://doi.org/10.1029/2021RG000768

References From the Supporting Information

Aitchison, J. (1989). Measures of location of compositional data sets. *Mathematical Geology*, *21*(7), 787–790. https://doi.org/10.1007/BF00893322

Rajič, K., Raimbourg, H., Famin, V., Moris-Muttoni, B., Fisher, D. M., Morell, K. D., & Canizarés, A. (2023a). Exhuming an accretionary prism: A case study of the Kodiak accretionary complex, Alaska, USA. *Tectonics*, *42*(10), e2023TC007754. https://doi.org/10.1029/2023TC007754

Woronow, A., & Love, K. M. (1990). Quantifying and testing differences among means of compositional data suites. *Mathematical Geology*, *22*(7), 837–852. https://doi.org/10.1007/BF00890666